J. Fluid Mech. (1996), *vol.* 309, *pp.* 277–300

The contraction of liquid filaments

By R. M. S. M. SCHULKES
Norsk Hydro a.s., Research Centre Porsgrunn, N-3901 Porsgrunn, Norway

(Received 6 January 1995 and in revised form 25 October 1995)

In this paper the evolution of a free liquid filament of arbitrary viscosity, contracting under the action of surface tension forces, is studied by numerical means. A finite-element discretization procedure is used to obtain approximate solutions to the Navier–Stokes equations. A Lagrangian approach is employed to deal with the large domain deformations which occur during the evolution of the filament. Typically we find that during the contraction a bulbous region forms at the end of the filament. The character of the evolution of the filament is found to be crucially dependent on the value of the Ohnesorge number Oh (a measure of viscous and surface tension forces). For large Ohnesorge numbers ($Oh \geqslant O(1)$) it is found that the liquid filament remains stable during contraction, even when the initial length of the filament is much longer than the Rayleigh stability limit. The bulbous end becomes more localized with decreasing Ohnesorge number while at the same time a clear neck forms in front of the bulbous end. In addition we find that the region in which the pressure is minimum moves towards the neck. For sufficiently small Ohnesorge numbers ($Oh \leqslant O(0.01)$) the filament becomes unstable with the radius of the neck decreasing and, eventually, the bulbous end breaking away from the filament.

1. Introduction

In a wide range of fluid dynamical processes long thread-like bodies of fluid may be formed. Unless constrained in some way, these threads of liquid (liquid filaments) will contract under the action of surface tension forces. The physical reason for the contraction is simply that surface tension forces try to minimize the surface energy by creating a spherical body of fluid. A simple contraction to a spherical domain does, however, not always occur. There is ample experimental evidence which shows that the filament may break up into separate parts during the contraction. Even in the case where the filament contracts without breakup occurring, the contraction is a complicated hydrodynamical process. It is the aim of this paper to increase our understanding of the contraction dynamics of liquid filaments with arbitrary viscosity.

In a discussion of previous experimental and theoretical work on the dynamics of liquid filaments, it is helpful to divide this work into two groups. The first group contains papers on what we will refer to as 'free filaments'. Free filaments evolve in a medium which has a neglegible viscosity compared with that of the fluid in the filament, and the outer medium is assumed to have no significant effect on the evolution of the filaments. Papers in the second group deal with filaments which are embedded in a fluid matrix which has a similar viscosity to that of the fluid in the filament. The evolution of such embedded filaments is significantly affected by the presence of the fluid matrix.

Let us first consider the dynamics of free filaments which often occur when a capillary surface breaks up in air. Such filaments occur, for example, in finite-length liquid jets (Goedde & Yuen 1970), bifurcating pendant drops (Hauser *et al.* 1936; Peregrin, Shoker & Symon 1990) and colliding drops (Jiang, Umemura & Law 1992). The experiments on liquid jets and bifurcating pendant drops show clearly the effect of viscosity on the contraction of the filament. Filaments consisting of high-viscosity fluids assume a characteristic dumb-bell shape during the contraction. The high-viscosity filaments contract fully to a spherical drop without breakup occurring. On the other hand, the contraction of a low-viscosity filament typically leads to large undulations on the filament. These undulations may be so large that the filament breaks up into separate drops before it has contracted fully. We point out that these undulations are not the result of the classical Rayleigh instability, but are capillary waves generated by the contraction of the end of the filament.

Attempts to model the evolution of free filaments are largely restricted to the limit of zero viscosity. In this limit the complexity of the governing equations reduces significantly owing to the fact that one has to solve Laplace's equation for the velocity potential rather than the full Navier–Stokes equations. Using a simplified model in which the end of a filament is assumed to consist of a blob of fluid connected to an inviscid thread, Keller (1983), and more recently, Ting & Keller (1990) and Keller, King & Ting (1995) predict that a thread of liquid with a uniform radius contracts with a uniform velocity. It is important to point out that this result assumes that a state of steady contraction exists, at least for some time during the contraction. It is, however, not certain that this is the case. In fact, the computations carried out in the present paper show that in the inviscid limit there is no state of steady contraction: the blob of fluid breaks away from the filament almost as soon as it has developed. Furthermore, as was pointed out earlier, large undulations occur on the surface of a contracting low-viscosity filament. The assumption that the filament consists of a bulbous end which is connected to a thread of fixed or monotonically increasing radius, is a rather severe approximation. Mansour & Lundgren (1990) have computed the contraction of short, inviscid filaments which result when a liquid jet breaks up. Their calculations clearly show the large undulations on the contracting filament. No breakup of the filament into separate drops is, however, observed, which might be because it was too short. In a recent numerical study of the bifurcation dynamics of a pendant drop, Schulkes (1994*b*) showed that a contracting filament-like body of inviscid fluid may in fact break up.

Taylor (1934) was one of the first to study the evolution of viscous drops embedded in another fluid. In recent years, the evolution of embedded liquid filaments has been studied extensively both experimentally and theoretically, see for example Stone, Bentley & Leal (1986) and Stone & Leal (1989) and the review paper by Stone (1994). Like in the case of free filaments, one of the interesting questions related to the evolution of the embedded liquid filament concerns the stability of the filament during the contraction. A liquid filament with a length longer than the Rayleigh stability limit (i.e. longer than the circumference of the filament) might break up into individual droplets. However, the time scale on which the filament contracts may be much smaller than the time scale on which the Rayleigh breakup occurs. While this would prevent the filament from breaking up due to the Rayleigh instability, there may be other mechanisms which lead to drop formation in the contracting filament. A particularly interesting observation in this respect emerged from the experimental study of Stone *et al.* (1986). They found that a liquid drop embedded in a fluid matrix could be extended significantly beyond the Rayleigh stability limit without breakup occurring due to the Rayleigh instability. Instead, it was found that during the contraction of the extended drop, bulbous ends would develop. If a bifurcation occurred, this bifurcation would almost without exception occur first at the bulbous end of the drop. This process was called 'end-pinching'. It is interesting that end-pinching is not restricted to high-viscosity, embedded liquid filaments. Inviscid, free filaments also exhibit end-pinching as shown by Schulkes (1994*b*).

In this paper we study the evolution of a free liquid filament of arbitrary viscosity. Experimental evidence suggests that viscosity is extremely important in relation to the evolution of the liquid filament. However, the desire to study the effects of viscosity prevents us from making any of the simplifying assumptions which significantly reduce the complexity of the problem both in the creeping flow (Stokes flow) limit and in the inviscid limit, namely that the governing equations can be reduced to integral equations defined only on the free boundary. In the intermediate-viscosity case this simplification is not possible and one is forced to work with the full nonlinear Navier–Stokes equations on a domain which deforms significantly in time.

Numerical techniques which have been developed to deal with hydrodynamic free-boundary problems fall in one of three catagories: Eulerian methods, Lagrangian methods and mixed Eulerian–Lagrangian methods. In the case of the Eulerian methods the computation is carried out on a fixed grid with the free boundary moving through the grid. One of the main difficulties associated with this method concerns the tracking of the moving boundary through the fixed grid, see e.g. Hirt & Nichols (1981). In the Lagrangian calculations nodal points are fixed to fluid particles and as a consequence the grid deforms during the computation. The Lagrangian methods in conjunction with finite-element techniques are very well suited to deal with free boundary problems for two reasons: the grid moves with the free boundary and the highly irregular domain which results is usually more conveniently treated with finite elements than with other discretization techniques. However, spatial variations in the convective velocity can lead to strong distortions of elements, often resulting in a breakdown of the calculations after some time, see for example Ramaswamy, Kawahara & Nakayama (1986). In order to try to combine the benefits of both the Eulerian and the Lagrangian approaches, arbitrary Lagrangian–Eulerian (ALE) techniques have been developed. ALE-based methods attempt to minimize the convective velocities thus preventing as much as possible the large element distortions in the Lagrangian approach while retaining the Lagrangian description of the moving free boundary. A clear exposition of the power of the ALE approach is given by Heurta & Liu (1988). In cases where the domain deforms in a global, more or less uniform manner, ALE-based methods have proved to be powerful. However, when large domain deformations occur on small length scales and at a position which is not known *a priori*, ALE-based methods lose much of their advantages over purely Lagrangian methods. Domain deformations can also be dealt with by means of a time-dependent map from the changing physical domain to a (fixed) computational domain. This approach has been applied successfully by Chen & Tsamopoulos (1993) to study nonlinear oscillations of liquid bridges. It is, however, likely to suffer from the same drawbacks as the Lagrangian approach: large local variations in the convective velocity will severely distort the physical domain so that regularity of the Jacobian of the transformations is not guaranteed.

In this paper we have opted for a finite-element discretization procedure in connection with an ALE-like approach to update to position of the nodal points in the mesh. Hence, the bounding surface of the mesh moves with the free (capillary) boundary. Details of the numerical approach are outlined in §3. Results of calculations are presented and discussed in §4 and §5 respectively.

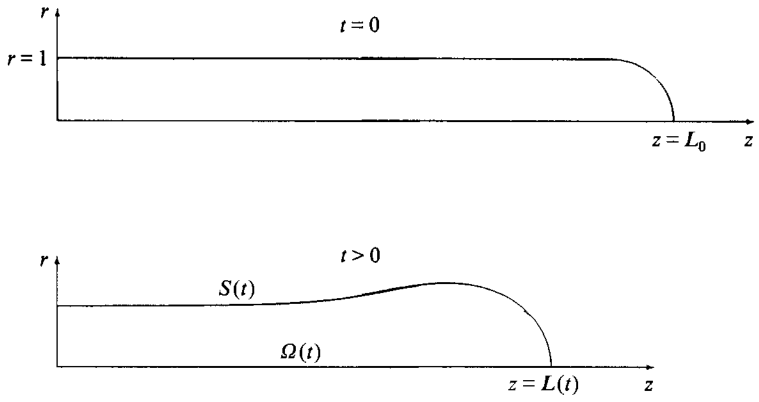

FIGURE 1. Schematic diagram and definition of variables.

2. Governing equations

It will be evident that when a liquid filament is formed in practice, the fluid inside the filament will not be stationary owing to the dynamics associated with the formation process. However, in order to gain some insight into the evolution of the liquid filament we make the important simplifying assumptions that at some time instant $t = 0$ the liquid filament is at rest and that its shape is known. Furthermore, it will be assumed that the filament consists of a long, axisymmetric, cylindrical body with rounded ends. The dimensionless radius of the filament at $t = 0$ is taken to be equal to $r = 1$ while the total dimensionless length of the fluid domain is equal to $2L_0$, cf. figure 1. For $t > 0$ the filament can contract freely under the action of surface tension forces. It follows that the axisymmetric fluid domain, denoted by $\Omega(t)$, and the bounding free surface denoted by $S(t)$ are time-dependent quantities.

Throughout this paper it will be assumed that the fluid under consideration is Newtonian and incompressible. In dimensionless form the governing equations are therefore the well-known Navier–Stokes equation

$$\frac{\partial \boldsymbol{u}}{\partial t} + (\boldsymbol{u} \cdot \nabla)\boldsymbol{u} + \nabla p = Oh \nabla^2 \boldsymbol{u} \quad \text{in } \Omega(t), \tag{1}$$

together with the incompressibility constraint

$$\nabla \cdot \boldsymbol{u} = 0 \quad \text{in } \Omega(t). \tag{2}$$

In the above equations $\boldsymbol{u}(r, z, t) = (u_r, u_z)$ denotes the dimensionless velocity field and $p(r, z, t)$ denotes the dimensionless pressure. The Laplace, gradient and divergence operators in (1) and (2) assume their respective forms in cylindrical polar coordinates. In order to obtain the dimensionless equations, the radius R of the cylindrical initial fluid domain was taken as a characteristic length scale, with γ/R denoting a pressure scale and $T = (\rho R^3/\gamma)^{1/2}$ a time scale (γ is the coefficient of surface tension and ρ is the fluid density). The only dimensionless group which appears is the Ohnesorge number, defined as $Oh = \nu(\rho/\gamma R)^{1/2}$ (ν denotes the kinematic viscosity). The Ohnesorge number is indicative of the relative importance of viscous and surface tension forces. Note, however, that the Ohnesorge number appears at the place where normally the Reynolds number appears. This suggests that the Ohnesorge number may also be regarded as the inverse of a Reynolds number of the flow. To show that this is indeed correct we only need to note that the ratio of inertia and surface tension forces, that is $\rho R U^2/\gamma$, is equal to unity when the velocity scale U is taken to be $U = R/T$.

The boundary conditions required to close the problem are as follows. On the symmetry axis $r = 0$ we have

$$u_r = 0, \quad \sigma_{rz} = 0, \tag{3}$$

while on the symmetry plane $z = 0$ the conditions

$$u_z = 0, \quad \sigma_{zr} = 0, \tag{4}$$

are prescribed. In (3) and (4) σ_{ij} denotes the usual Cauchy stress tensor in which the viscosity coefficient is replaced by the Ohnesorge number. Incorporating the (constant) ambient pressure in the pressure p and assuming that the medium outside $\Omega(t)$ is unable to resist fluid motion on $S(t)$, it follows that the normal and tangential stresses on the capillary surface are given by

$$\sigma_n = 2\mathscr{H}, \quad \sigma_\tau = 0 \quad \text{on} \quad S(t). \tag{5}$$

In the above equations $2\mathscr{H}$ denotes the total curvature of the surface $S(t)$, $\sigma_n = \sum_{i,j=1}^{2} \sigma_{ij} n_i n_j$ and $\sigma_\tau = \sum_{i,j=1}^{2} \sigma_{ij} n_i t_j$ with $n_i, t_i, i = 1,2$ denoting components of the unit normal and unit tangential vectors respectively on $S(t)$. The final condition to be prescribed on the capillary surface is the kinematic condition which specifies that the free surface is a material surface, thus

$$\frac{\mathrm{D}\boldsymbol{x}}{\mathrm{D}t} = \boldsymbol{u} \quad \text{on} \quad S(t), \tag{6}$$

with $\mathrm{D}/\mathrm{D}t$ denoting the usual convective derivative.

3. Numerical implementation

3.1. *Spatial discretization*

In order to employ the finite-element method, the weak formulation of the problem specified by equations (1)–(5) is required. The weak (or variational) formulation is obtained in the usual way by multiplying (1) and (2) by sufficiently smooth test functions $\boldsymbol{v}$ and q, and using partial integration to reduce the order of differentiation. On using the boundary conditions (3), (5) we find after some algebra that the variational form of the momentum equation (1) reads

$$\int_{\Omega(t)} \left[\boldsymbol{v} \cdot \left(\frac{\partial \boldsymbol{u}}{\partial t} + (\boldsymbol{u} \cdot \nabla)\boldsymbol{u} \right) + p \nabla \cdot \boldsymbol{v} \right] r \mathrm{d}r \mathrm{d}z + Oha(\boldsymbol{u}, \boldsymbol{v}) = \int_{S(t)} 2\mathscr{H} v_n r \mathrm{d}s, \tag{7}$$

in which

$$a(\boldsymbol{u}, \boldsymbol{v}) = \int_{\Omega(t)} \left(2 \left(\frac{\partial u_r}{\partial r}\frac{\partial v_r}{\partial r} + \frac{u_r v_r}{r^2} + \frac{\partial u_z}{\partial z}\frac{\partial v_z}{\partial z} \right) + \left(\frac{\partial u_r}{\partial z} + \frac{\partial u_z}{\partial r} \right) \left(\frac{\partial v_r}{\partial z} + \frac{\partial v_z}{\partial r} \right) \right) r \mathrm{d}r \mathrm{d}z. \tag{8}$$

The quantity $Oha(\boldsymbol{u}, \boldsymbol{v})$ is a measure of the rate of dissipation of energy due to viscous forces in the fluid domain. The curvature term in the boundary integral in (7) contains second-order derivatives which may be removed in the following manner. The total curvature of the surface $S(t)$ can be written as

$$2\mathscr{H}\boldsymbol{n} = -\frac{\partial \boldsymbol{t}}{\partial s} + \frac{1}{R_2}\boldsymbol{n}, \tag{9}$$

in which $\boldsymbol{n}$, $\boldsymbol{t}$ denote unit normal and tangential vectors to $S(t)$ and

$$\frac{1}{R_2} = \frac{z_s}{r(r_s^2 + z_s^2)^{1/2}}, \tag{10}$$

with the subscript s denoting a derivative along the arclength of the surface $S(t)$. Hence, using (9) and partial integration we find that the surface integral in (7) can be written as

$$\int_{S(t)} 2\mathscr{H} v_n r \mathrm{d}s = \int_{S(t)} \frac{1}{R_2} v_n r \mathrm{d}s + \int_{S(t)} \boldsymbol{t} \cdot \frac{\partial}{\partial s}(\boldsymbol{v} r) \mathrm{d}s. \tag{11}$$

The continuity equation (2) is treated in the following way. Rather than working with the continuity equation as it stands, this equation is perturbed by adding a small (penalty) term containing the pressure, via

$$\epsilon p + \nabla \cdot \boldsymbol{u} = 0, \tag{12}$$

or in variational form

$$\epsilon \int_{\Omega(t)} pq r \mathrm{d}r \mathrm{d}z + \int_{\Omega(t)} q \nabla \cdot \boldsymbol{u} r \mathrm{d}r \mathrm{d}z = 0. \tag{13}$$

The parameter ϵ is small (we have taken $\epsilon = 10^{-9}$) so that the term ϵp in the perturbed continuity equation effectively introduces some artificial compressibility. The reason for perturbing equation (2) is the following. Using the unperturbed continuity equation (2) leads after discretization to a system of equations which either has a large bandwidth or allows the possibility of zeros on the leading diagonal. The large bandwidth reduces the efficiency of any matrix solver, while the possibility of zeros on the leading diagonal requires the use of partial pivoting which is expensive numerically. These difficulties are overcome by using the perturbed continuity equation (12) (for details refer to Cuvelier, Segal & Van Steenhoven 1986)

Using (7), (11) and (13) we find that the variational formulation of the momentum equation and the perturbed continuity equation as follows.

Find $\boldsymbol{u}$, $p \in \Omega(t)$ such that for all sufficiently smooth functions $\boldsymbol{v}$, $q \in \Omega(t)$ the following equations are satisfied:

$$\left.\begin{aligned} \int_{\Omega(t)} \left(\boldsymbol{v} \cdot \left(\frac{\partial \boldsymbol{u}}{\partial t} + (\boldsymbol{u} \cdot \nabla)\boldsymbol{u} \right) + p \nabla \cdot \boldsymbol{v} \right) r \mathrm{d}r \mathrm{d}z + Oh a(\boldsymbol{u}, \boldsymbol{v}) &= \int_{S(t)} \frac{1}{R_2} v_n r \mathrm{d}s + \int_{S(t)} \boldsymbol{t} \cdot \frac{\partial}{\partial s}(\boldsymbol{v} r) \mathrm{d}s, \\ \epsilon \int_{\Omega(t)} pq r \mathrm{d}r \mathrm{d}z + \int_{\Omega(t)} q \nabla \cdot \boldsymbol{u} r \mathrm{d}r \mathrm{d}z &= 0. \end{aligned}\right\} \tag{14}$$

With the exception of the kinematic boundary condition (6) all boundary conditions are incorporated in (14).

In order to construct a discrete system of equations the domain $\Omega(t)$ is divided up into triangular elements. On each element the velocity $\boldsymbol{u}$ and the pressure p are approximated by a linear combination of the usual finite-element basis functions with compact support. The basis functions $\phi_i(r, z)$ for the velocity components are members of the family of extended quadratic polynomials (based on the three vertices, the three midpoints of the sides and the barycentre of the triangle). The basis functions $\psi_i(r, z)$ for the pressure are in the family of linear polynomial functions (based on one nodal point including two derivatives). Thus on each element we have the approximations

$$\tilde{\boldsymbol{u}}(r, z, t) = \sum_{i=1}^{7} \boldsymbol{u}_i(t) \phi_i(r, z), \quad \tilde{p}(r, z, t) = \sum_{i=1}^{3} p_i(t) \psi_i(r, z), \tag{15}$$

in which $\boldsymbol{u}_i = (u_{ri}, u_{zi})$ and p_i are values of the velocity and the pressure respectively at the nodal points. Substituting the above approximations of the velocity and the pressure on each triangular element into (14), using as test functions $\boldsymbol{v} = (\phi_j, \phi_j)$ and

$q = \psi_j$ and adding the contributions from all elements, we obtain the discrete systems of equations

$$\left.\begin{aligned} &\boldsymbol{M}\frac{\partial \hat{\boldsymbol{u}}}{\partial t} + \boldsymbol{C}(\hat{\boldsymbol{u}})\hat{\boldsymbol{u}} - \boldsymbol{L}^T\hat{\boldsymbol{p}} + Oh\boldsymbol{A}\hat{\boldsymbol{u}} = \boldsymbol{f}, \\ &\epsilon\boldsymbol{D}\hat{\boldsymbol{p}} = -\boldsymbol{L}\hat{\boldsymbol{u}}. \end{aligned}\right\} \tag{16}$$

In the above equations $\hat{\boldsymbol{u}}$ and $\hat{\boldsymbol{p}}$ denote vectors which contain velocity and pressure unknowns respectively at the nodal points. The matrices $\boldsymbol{M}$, $\boldsymbol{C}$, $\boldsymbol{L}$, $\boldsymbol{A}$ and $\boldsymbol{D}$ are called the mass, convective, pressure, stiffness and pressure-mass matrices respectively and $\boldsymbol{f}$ is the force vector resulting from the surface integrals in (14). The pressure-mass matrix $\boldsymbol{D}$ is non-singular so that it may be inverted and hence the pressure can be expressed explicitly in terms of the velocity unknowns by means of the perturbed continuity equation. The system of equations which results after eliminating the pressure reads

$$\boldsymbol{M}\frac{\partial \hat{\boldsymbol{u}}}{\partial t} + \boldsymbol{C}(\hat{\boldsymbol{u}})\hat{\boldsymbol{u}} + \boldsymbol{S}\hat{\boldsymbol{u}} = \boldsymbol{f}, \tag{17}$$

in which

$$\boldsymbol{S} = Oh\boldsymbol{A} + \frac{1}{\epsilon}\boldsymbol{L}^T\boldsymbol{D}^{-1}\boldsymbol{L}.$$

Without going into details we point out that the matrix $\boldsymbol{S}$ can be assembled efficiently, that it retains the properties of the matrix $\boldsymbol{A}$ (symmetry and positive definiteness) and that its bandwidth does not differ significantly from that of the matrix $\boldsymbol{A}$. All further specific details of the discretization procedure will be omitted since the method is well-established. Information concerning the application of the finite-element method to the Navier–Stokes equations, including the penalty function approach can be found in Cuvelier *et al.* (1986).

3.2. *Time integration*

Owing to the presence of the convective term $\boldsymbol{C}(\hat{\boldsymbol{u}})\hat{\boldsymbol{u}}$, the system of equations (17) is nonlinear in $\hat{\boldsymbol{u}}$. Further nonlinearities arise from the curvature terms which are contained in the forcing vector $\boldsymbol{f}$. Clearly, solving the nonlinear system of equations exactly (to within numerical accuracy) at each time step would require an iterative solution technique. However, this is computationally expensive given the fact that each iteration would involve a deformation of the domain with associated computational costs. Hence, in order to reduce the computational time we use the following commonly adopted approach. The convective term is linearized by using Picard linearization (successive substitution) and it is assumed that for a sufficiently small time step Δt the function values at the previous time step provide a good initial guess so that no iteration is required. Furthermore, given Ω^n, the domain at some time $t^n = n\Delta t$, we calculate the velocity field at $t = t^{n+1}$ on Ω^n and the domain deformation is calculated subsequently as outlined below. The system of equations (17) is integrated in time using the θ-method which, on applying the Picard linearization of the convective term, yields

$$\boldsymbol{M}\frac{\hat{\boldsymbol{u}}^{n+\theta} - \hat{\boldsymbol{u}}^n}{\Delta t} + \boldsymbol{C}(\hat{\boldsymbol{u}}^n)\hat{\boldsymbol{u}}^{n+\theta} + \boldsymbol{S}\hat{\boldsymbol{u}}^{n+\theta} = \boldsymbol{f}^n, \tag{18}$$

in which $\hat{\boldsymbol{u}}^n = \hat{\boldsymbol{u}}(t^n)$ and $\hat{\boldsymbol{u}}^{n+\theta} = \theta\hat{\boldsymbol{u}}^{n+1} + (1-\theta)\hat{\boldsymbol{u}}^n$ $(0 \leqslant \theta \leqslant 1)$. Note that the force vector $\boldsymbol{f}$ at the time level t^n is used rather than at level $t^{n+\theta}$. In our calculations we will always take θ in the range $0.5 < \theta < 1$ since the θ-method is unconditionally stable in this interval, see e.g. Lambert (1991). Owing to the fact that $\boldsymbol{f}^n$ is used rather than $\boldsymbol{f}^{n+\theta}$, the discretization error of (18) is of order Δt for all values of $\theta \in [0, 1]$.

3.3. *Domain deformations*

Suppose the velocity field $\hat{\boldsymbol{u}}^{n+1}$ is calculated using (18) on the domain Ω^n. The new free-surface position is then calculated in the following way. The position vector of the free boundary $\boldsymbol{x}_S^n$ is known and the nodal points on the boundary are now updated by applying the kinematic condition (6). Using a simple first-order Euler scheme for the kinematic condition yields

$$\boldsymbol{x}_S^{n+1} = \boldsymbol{x}_S^n + \Delta t \hat{\boldsymbol{u}}_S^{n+1}. \tag{19}$$

Once the deformation of the free boundary is known, a new mesh is calculated such that changes in the mesh reflect the topological changes of the free boundary. Rather than interpolating the function values between the old nodal points to obtain function values at the new nodal points, the function values at the new nodal points are just taken to be those at the old nodes. This approach may be justified as follows. Nodes move a distance of order $U\Delta t$ where U is a dimensionless velocity scale. Approximating function values at the new nodal positions by using those at old nodes introduces a spatial discretization error of order Δt. The overall accuracy of the numerical implementation is not reduced by this approximation since this spatial discretization error is of the same order as the discretization error in the time integration scheme (18). Note that when $U \gg 1$ we have to reduce Δt in order to maintain accuracy. Numerical experiments show, however, that $U \sim 1$ in most cases we have considered.

Numerical experiments were carried out where interpolation was used to calculate the solution at the new mesh. The relative difference between the solution obtained with and without interpolating was so small (typically $< 1\%$) that the extra computational cost of interpolating the solution was not warranted. Furthermore, interpolation has a diffusive effect on the solution. It can be shown that the amount of diffusion due to interpolation is of the order $Uh\Delta t$, in which h is a typical diameter of an element. In order for numerical diffusion to be negligible compared with physical diffusion we therefore require $Uh\Delta t \ll Oh$. While in all numerical experiments presented in the following sections this condition was satisfied, the extra constraint on the time step may be quite restrictive for small values of Oh when interpolation is used.

The time integration scheme as given by (18) and (19) for the free-boundary problem under consideration does not require an iterative procedure at each time step: $\hat{\boldsymbol{u}}^{n+1}$ is calculated explicitly and the domain is updated subsequently. In order to test the accuracy of this approach, the following iterative scheme was also implemented. Given Ω^n, the approximation $\hat{\boldsymbol{u}}^{(1)}$ to $\hat{\boldsymbol{u}}^{n+1}$ was calculated using (18). Subsequently the domain was deformed using (19), new matrices and a new right-hand-side vector $\boldsymbol{f}$ are calculated and a new approximation $\hat{\boldsymbol{u}}^{(2)}$ to $\hat{\boldsymbol{u}}^{n+1}$ is found. This process was repeated until the relative difference (in the 2-norm) between successive approximations of $\hat{\boldsymbol{u}}^{n+1}$ was less than 0.1%. It was found that generally only two steps in this iterative procedure were required in order to obtain the desired accuracy. These results justify our approach of assuming that the first approximation to $\hat{\boldsymbol{u}}^{n+1}$ is sufficiently accurate. As with the interpolation, the slightly increased accuracy obtained by applying the iterative procedure does not warrant the huge increase in the computational cost and hence the iterative procedure is not applied.

As an example of the domain deformation we are capable of dealing with, figure 2 shows the initial (*a*), intermediate (*b*) and the final (*c*) mesh resulting from a simulation

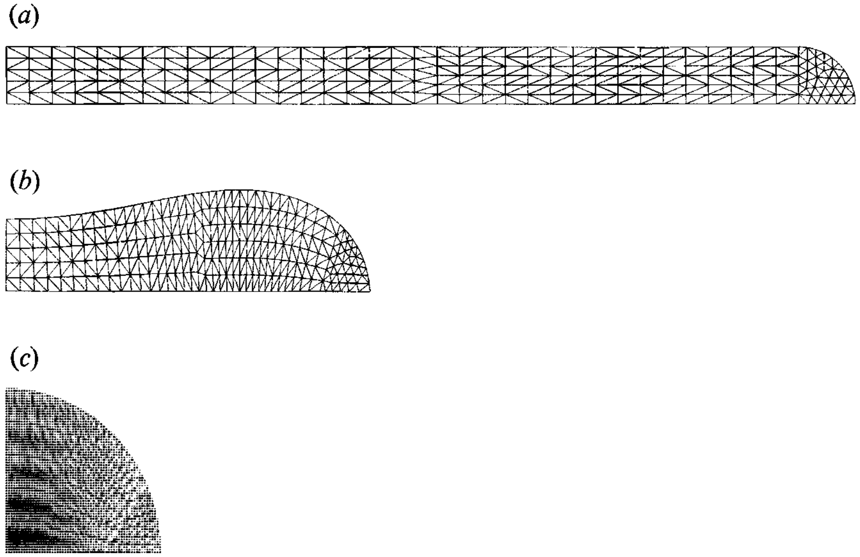

FIGURE 2. Examples of typical domain deformations and the corresponding evolution of the mesh. The meshes shown correspond to the initial (*a*), intermediate (*b*) and final (*c*) stages of a computation with $L_0 = 15$ and $Oh = 1$.

in which $Oh = 1$ and the initial half-length $L_0 = 15$. Note that only one quarter of the domain is plotted owing to the axial symmetry and the symmetry about the plane $z = 0$.

3.4. *Numerical tests*

It is imperative to test our numerical implementation before we proceed with the liquid filament problem. We do this by considering a slightly extended drop which we allow to relax to its spherical shape. For sufficiently small values of the Ohnesorge number Oh the drop will oscillate and the amplitude of the oscillations decreases owing to the action of viscous forces. The high-frequency modes will be damped most strongly so that after some time we expect the drop to oscillate with the frequency of the fundamental mode with amplitudes decreasing exponentially with time. For sufficiently large values of Oh the viscous forces are dominant and we expect to observe an aperiodic damping process. In figure 3 we have plotted the position of the free-surface node situated on the symmetry axis as a function of time for the cases $Oh = 0.05$ and $Oh = 1$. The initial configuration of the drop was taken to be a cylindrical body of unit length with spherical caps of unit radius at each end of the cylinder. The domain was discretized using 306 elements. We note the oscillatory decay of the amplitude in the case $Oh = 0.05$ while for $Oh = 1$ the decay is clearly monotonic which is in agreement with our expectations. The equilibrium attained by the drop when oscillations have damped out provides a good test of mass conservation of the numerical code. We find that for $Oh = 1$ the equilibrium radius at $t = 30$ is equal to $R = 1.35737$ while the theoretical equilibrium radius is given by $R = (5/2)^{1/3} = 1.35725$. In the present example the total mass change during the calculation is less than 0.01%. In all subsequent calculations we have chosen the number of elements in the finite-element mesh such that the total mass change during the calculation was less than 0.1%. From the positions and the amplitudes of the maxima in figure 3 we can readily determine the frequency of oscillations and the rate

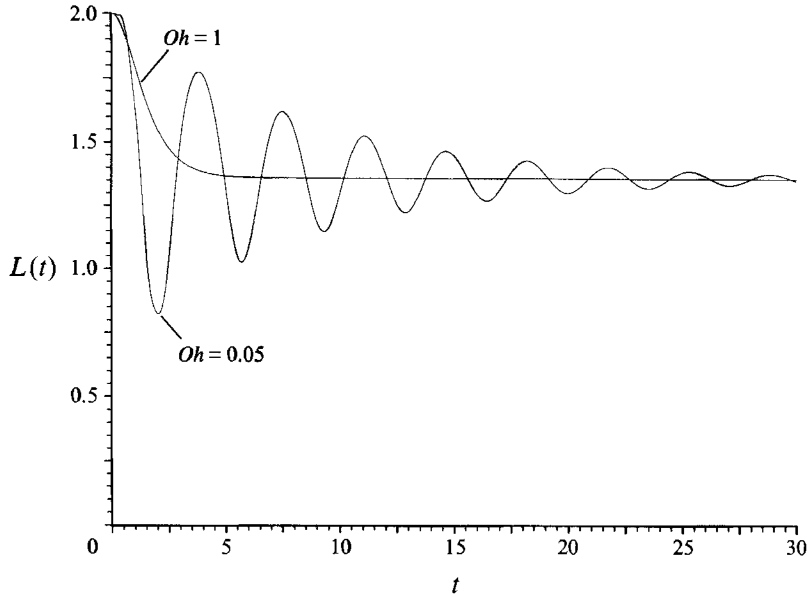

FIGURE 3. The position of the free-surface node on the symmetry axis as a function of time for the Ohnesorge numbers as indicated in the plot.

ω	δ
1.712	0.127
1.745	0.124
1.763	0.123
1.770	0.122
1.773	0.122
1.773	0.122
1.774	0.123

TABLE 1. The frequency ω and damping coefficient δ as calculated from successive maxima in figure 3.

of decay of the oscillations. In the case of $Oh = 0.05$, eight maxima are distinguishable in the time interval $[0, 30]$. The frequencies ω and rates of decay δ as derived from positions and amplitudes at successive maxima in figure 3 are listed in table 1. We note that as time progresses (moving down the table), the frequencies increase. This is in qualitative agreement with analytical work by Tsamopoulos & Brown (1983), who showed that the frequency of oscillations increases with decreasing amplitudes of the oscillations. In the limit of infinitesimal oscillations the frequencies should tend asymptotically to the eigenfrequencies of a drop as obtained from linear theory. The frequencies of an oscillating viscous drop were calculated by Reid (1960) for arbitrary viscosity. In Appendix A it is shown that for small Ohnesorge numbers the dimensionless frequency (ω) and damping coefficient (δ) of a drop are approximated by $\omega = 1.775$ and $\delta = 0.122$. Clearly, these results agree well with those obtained from computations as presented in table 1.

The effect of the artificial compressibility which was introduced to deal with the continuity equation (refer to (13)) was also investigated. It was found that for $\epsilon \leqslant 10^{-6}$ there was no discernible change in the test results mentioned in this section. Thus, taking $\epsilon = 10^{-9}$ as we have done in our calculations, guarantees that effects of the artificial compressibility are negligible.

4. Results of computations

Let us start our investigation into the contraction of liquid filaments by studying the dependence of the contraction on the Ohnesorge number Oh. In all cases we take the initial domain to consist of a cylinder with unit radius bounded by a spherical cap. The initial half-length of the filament is taken to be $L_0 = 15$ (aspect ratios of $O(10)$ are not unusual for low-viscosity fluids while for high viscosity the aspect ratio may be up to one order of magnitude larger, see Zhang & Basaran, 1995). At $t = 0$ the filament is at rest and for $t > 0$ it can contract freely under the action of surface tension forces. In all calculations we have taken $\theta = 0.7$ and $\Delta t = 0.01$ when $Oh \geqslant 0.1$ while $\Delta t = 0.005$ when $Oh < 0.1$. Let us first consider the case in which $Oh = 1$. The domain deformation together with vector plots of the velocity field and contour plots of the pressure are shown in figures 4(*a*) and 4(*b*) respectively, at the times indicated in the plots. We observe that at $t = 3$ a bulbous end has formed with a radius somewhat larger than that of the initial filament. The vector field shows that the filament contracts without the occurrence of large velocity gradients. The pressure contours at $t = 3$ show that a pressure minimum is situated near the inflection point of the second derivative of the function $f(z)$, where $r = f(z)$ denotes the instantaneous free-surface shape. This is an important observation since the point of inflection corresponds to a minimum in the normal stress jump across the interface (cf. Stone *et al.* 1986, figure 14). We observe in figure 4 that the pressure field remains unchanged during the contraction until the bulbous end meets the symmetry plane. The pressure contours in figure 4(*b*) are typical for filaments with Ohnesorge number $Oh \geqslant \mathrm{O}(1)$. It follows that for large Ohnesorge numbers the pressure in the filament during contraction is mainly determined by the normal stress jump across the free surface.

From figure 4 it is clear that end-pinching, the separation of the bulbous end from the filament, does not occur in the case with $Oh = 1$. In fact with $Oh = 1$ end-pinching was never observed in our numerical experiments (the evolution of filaments with initial lengths up to $L_0 = 30$ was studied). The Rayleigh instability was also not observed, even though the initial length of the filament was up to ten times the Rayleigh stability limit. Evidently, the time scale on which the Rayleigh instability will manifest itself was large compared with the time scale on which the filament contracts. We should point out that the absence of the Rayleigh instability may be an artifact of the initial conditions which we have assumed at $t = 0$, namely that the liquid filament was perfectly cylindrical and completely at rest. It follows that the only perturbations introduced are those associated with numerical round-off. While these perturbations should, eventually, lead to the growth of the Rayleigh instability, the time scales required to do so are (artificially) long. It will be clear that in any real-life situation large perturbations are likely to be present which may lead to the Rayleigh breakup before the filament has contracted. However, we are not aware of experimental evidence of Rayleigh breakup in a contracting free filament.

Before we proceed to study the evolution of the filament for a different Ohnesorge number, let us compare our results so far with the experimental study by Stone *et al.* (1986). In this study the evolution of extended drops embedded in a fluid matrix was investigated. One of the important parameters is the viscosity ratio of the drop viscosity μ and the matrix viscosity μ/λ. In the limit $\lambda \to \infty$ the viscosity of the

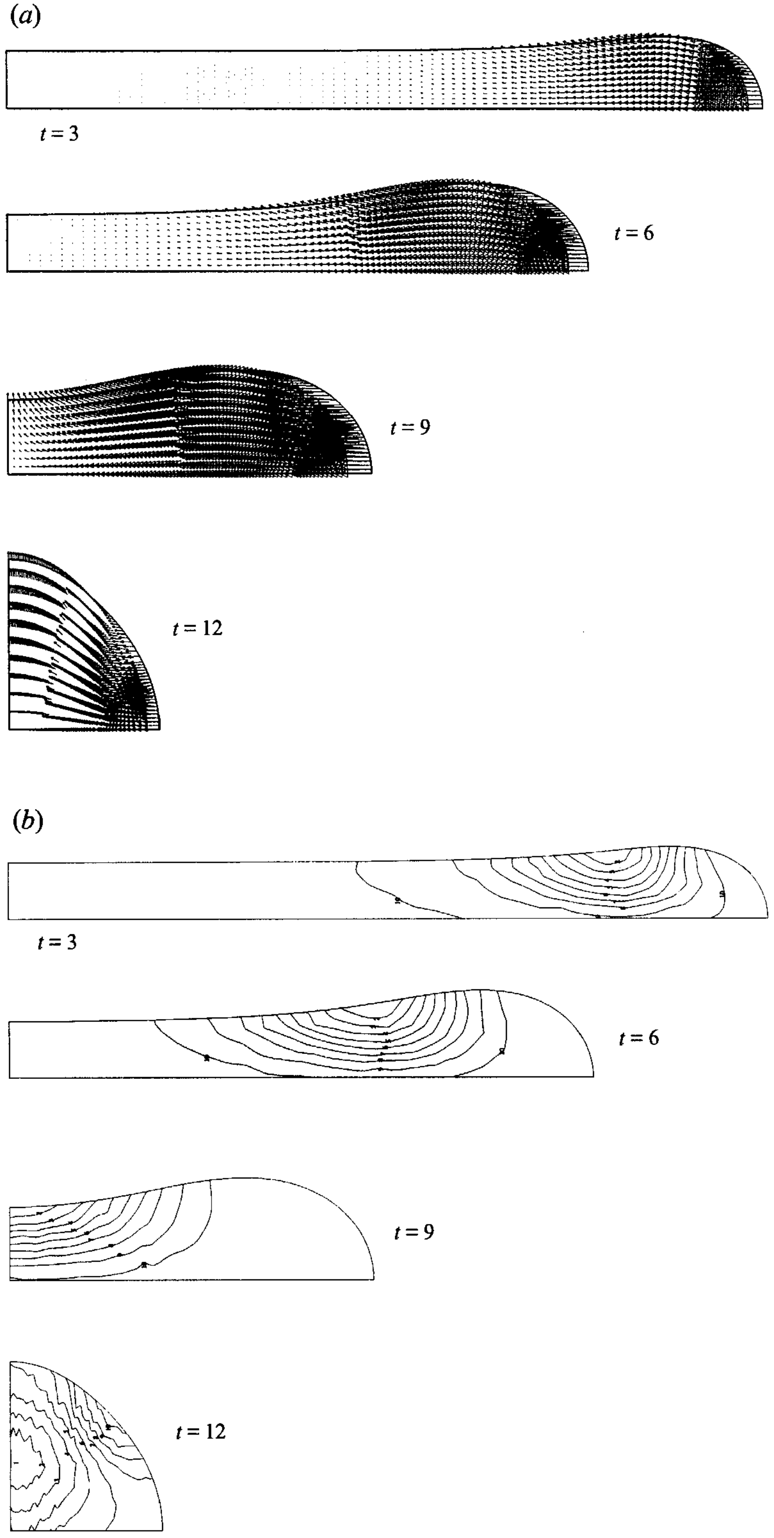

FIGURE 4. The evolution of a liquid filament with $L_0 = 15$ and $Oh = 1$. Vector plots of the velocity field (*a*) and contour plots of the pressure (*b*) are shown at the times $t = 3, 6, 9, 12$ as indicated.

fluid matrix is negligible compared with that of the drop. This is the limit which corresponds to our study of free liquid filaments when inertia effects of the outer fluid are discarded. In their experiments, Stone *et al.* found that for large values of λ (that is $\lambda \sim O(10)$) a highly elongated drop ($L_0 \approx 35$) could contract without either end-pinching or the Rayleigh instability leading to breakup. Smaller values of λ would typically give rise to end-pinching. It was also found that the drop would have to be elongated to up to ten times the Rayleigh stability limit in order for the Rayleigh instability to appear. These results are in broad agreement with our calculations with $Oh \geqslant O(1)$. Furthermore, the shape of the contracting filament in the experiment with $\lambda \sim O(10)$ is very similar to that observed in figure 4. The results suggest that viscous effects of the outer fluid do not change the qualitative features of the contracting embedded filament as compared with a contracting free filament when the Ohnesorge number is sufficiently large.

Let us next consider the case in which $Oh = 0.1$ with $L_0 = 15$ as before. Vector plots of the velocity field and contour plots of the pressure are presented in figure 5. In this case it was possible to continue the time integration until the point at which the bulbous end of the filament reached the symmetry plane. At that point the axial momentum of the contacting filament is transferred in the radial direction, leading to a flattened drop with a rapidly increasing radius. The mesh adaptation routine which we have used is unable to cope with this large and rapid domain deformation and consequently the calculation had to be terminated at this point. When the evolution of the filament with $Oh = 0.1$ is compared with $Oh = 1$, we find a number of important qualitative differences. The most obvious difference is the increase in the radius and the more pronounced, rounded shape of the bulbous end. In addition we note that decreasing the Ohnesorge number has led to the formation of a clear neck and a small wave-like disturbance moving ahead of the neck. We observe, furthermore, that whereas in the case with $Oh = 1$ the velocity gradients were small, with $Oh = 0.1$ large velocity gradients occur. In the case with $Oh = 1$ all velocity vectors point in the same direction (all the fluid is pushed ahead of the contracting end) while with $Oh = 0.1$ fluid from the neck is sucked into the bulbous end and at least two stagnation points are visible on the symmetry axis.

When we turn our attention to the pressure contours in figure 5(*b*) we observe other significant differences as compared with figure 4(*b*). Clearly the pressure gradients are much larger with $Oh = 0.1$ and, significantly, the point of minimum pressure has shifted from the first point of inflection (as seen from the bulbous end of the filament) towards the neck. Thus, while with $Oh = 1$ the pressure distribution is determined by the normal stress jump across the free surface, when $Oh = 0.1$ the dynamics of the fluid motion affects the pressure distribution significantly. The shift of the pressure minimum can be explained as follows. Assuming that we can make the approximation $\sigma_n = -p + 2Oh\,\partial u_n/\partial n$ (which is stricktly speaking valid only when $\nabla \cdot \boldsymbol{n} \approx 0$), the normal stress condition as given by (5) becomes

$$-p + 2Oh\frac{\partial u_n}{\partial n} = 2\mathscr{H}. \tag{20}$$

When we concentrate on the neck region in figure 5(*a*) we observe that on the bulbous side of the neck $\partial u_n/\partial n > 0$ (the component of the velocity normal to the surface increases towards the surface) while $\partial u_n/\partial n < 0$ on the other side of the neck. This implies that dynamic effects increase the pressure near the point of inflection while the pressure is lowered towards the neck which is in accordance with observations. However, notwithstanding the large qualitative change in the character of the flow

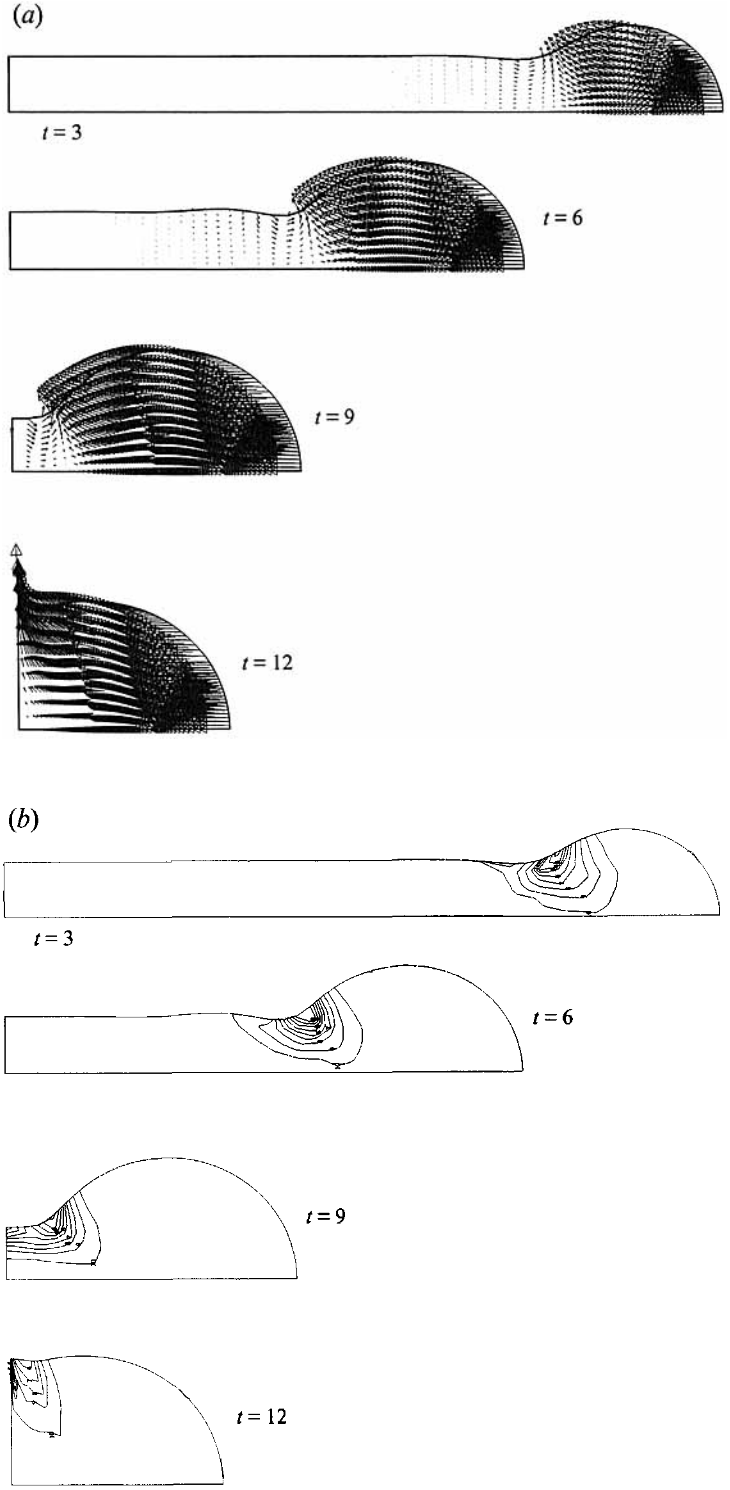

FIGURE 5. The evolution of a liquid filament with $L_0 = 15$ and $Oh = 0.1$. Vector plots of the velocity field (*a*) and contour plots of the pressure (*b*) are shown at the times $t = 3, 6, 9, 12$ as indicated.

and pressure field which occurs when the Ohnesorge number is lowered from $Oh = 1$ to $Oh = 0.1$, in neither case did end-pinching occur nor did the Rayleigh instability appear.

Lowering the Ohnesorge number further to $Oh = 0.01$ leads to an interesting qualitative change in the evolution of the filament. In figure 6 we have plotted the velocity vector field and the pressure contours at the times indicated in the plots. We note that the neck, which first appeared with $Oh = 0.1$, has become more pronounced while a clear wave-like disturbance is generated ahead of the neck. The calculations of Mansour & Lundgren (1990) show that in the inviscid limit a similar wave-like disturbance is generated on the surface of a filament. When contour plots of the pressure are considered we observe that at $t = 1$ there are two pressure minima. The minima have merged at $t = 2$ and subsequently the pressure minumum becomes highly localized in the neck. Unfortunately we are unable to continue the numerical integration after $t = 4.31$ due to the large distortions of the mesh in the neck region. This distortion of the mesh is the result of the large curvature of the surface in the neck coupled with a large gradient in the velocity along the free surface (recall that the update of the mesh is based on changes which occur along the free boundary). A doubling of the number of elements in the mesh enabled us to continue the integration only until $t = 4.39$. The numerical problems which we experience are typical for (capillary) free-boundary problems in which large changes in the curvature may coincide with large velocity gradients over small length scales. Even in the case where the more flexible boundary-element technique is used, localized regions in which large changes in the curvature occur are often the source of numerical difficulties (see e.g. Schulkes 1994*a*).

When the results for $Oh = 0.01$ are compared with the previous results obtained with $Oh = 1, 0.1$ we observe the following trends. Lowering the Ohnesorge number leads to the formation of a more localized, rounded bulbous end of the contracting filament. A neck which forms in front of the contracting bulbous end becomes deeper and more localized when the Ohnesorge number is lowered. Furthermore, while the pressure for large Ohnesorge numbers is mainly determined by the normal stress jump across the free surface, for small Ohnesorge numbers the pressure is determined significantly by dynamic effects and as a consequence the pressure minumum moves towards the neck. It is interesting to point out that as the Ohnesorge number is lowered, the neck region appears to act increasingly as a Venturi tube: large flow speeds in the neck lower the pressure in the neck. The question now arises of whether the numerical difficulties experienced in the case of $Oh = 0.01$ are in any way related to the onset of end-pinching. Namely, as the radius of the neck decreases the normal stress jump across the free surface will increase in the neck. This fact, together with our observation that the pressure decreases in the neck owing to dynamic effects, ensures that the mechanisms for end-pinching to occur are in place. However, since we are unable to continue the calculation until the point at which the radius of the neck vanishes, we are not able to determine with certainty whether or not end-pinching occurs.

5. Discussion

5.1. *End-pinching*

In the previous section it was shown that a decrease in the Ohnesorge number Oh leads to the formation of an increasingly localized and pronounced necking region. However, owing to numerical constraints brought about by the severe deformation of

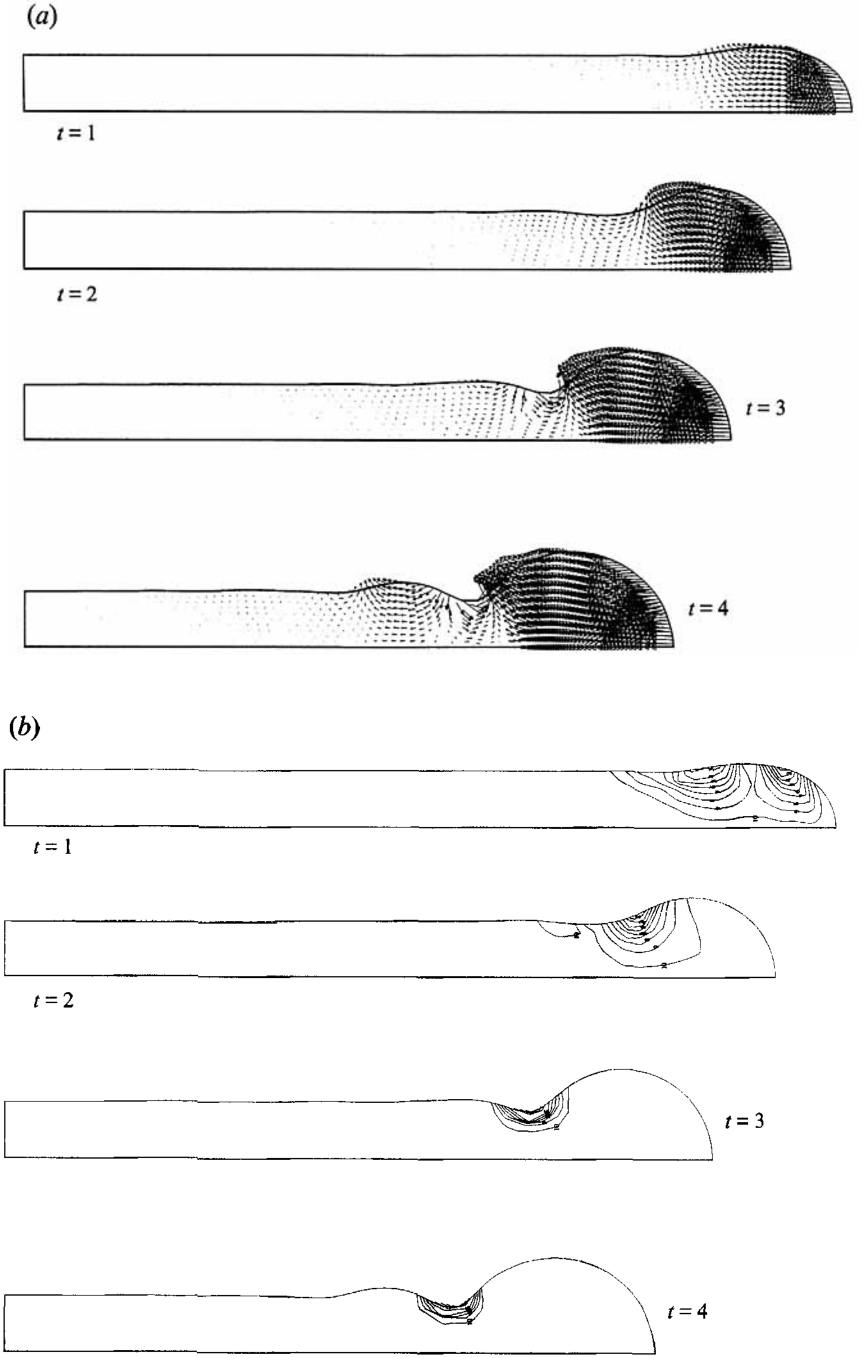

FIGURE 6. The evolution of a liquid filament with $L_0 = 15$ and $Oh = 0.01$. Vector plots of the velocity field (*a*) and contour plots of the pressure (*b*) are shown at the times $t = 1, 2, 3, 4$ as indicated.

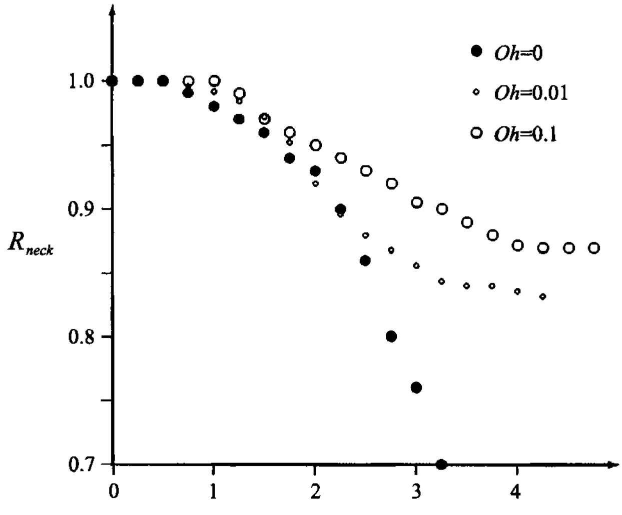

FIGURE 7. A plot of the radius of the neck as a function of time for the parameters $L_0 = 15$ and $Oh = 0.1, 0.01$ and 0 (velocity potential calculation).

the mesh in the necking region, we were unable to determine with certainty whether or not end-pinching will occur. All we are able to say is that for $Oh \geqslant O(0.1)$ end-pinching will not occur. In order to shed more light on the question of end-pinching for free liquid filaments we have used a boundary-element code which was employed in earlier calculations (Schulkes 1994*a*) to investigate the contraction of an inviscid liquid filament. Results of one of these calculations in which $L_0 = 15$ are presented in Appendix B. It is found that in the inviscid limit end-pinching will indeed occur. This result appears to confirm the trend which emerged from the calculations in the previous section (a lower Ohnesorge number leads to a more pronounced neck). However, the question now arises of whether or not there is a 'critical' Ohnesorge number Oh^* such that end-pinching occurs for $Oh < Oh^*$ while no end-pinching occurs for $Oh > Oh^*$. In order to attempt to answer this question let us consider the radius of the neck as a function of time. In figure 7 the radius of the neck versus time is plotted for the Ohnesorge numbers $Oh = 0.01, 0.1$ and for the inviscid case. In the inviscid limit we observe that a neck starts to form after $t = 0.75$ after which the radius of the neck decreases with an inceasing rate. When the viscosity is finite we notice that the neck takes somewhat longer to appear than in the inviscid limit. In the case of $Oh = 0.1$ the neck begins to appear at $t = 1$ after which the radius of the neck decreases steadily. However, after $t = 4$ the radius of the neck appears to attain a more or less steady value at approximately 88% of the undisturbed radius. Decreasing the Ohnesorge number to $Oh = 0.01$ we see the same qualitative behaviour as with $Oh = 0.1$ with the difference that the 'steady' radius of the neck has formed earlier and has reduced to 85% of the undisturbed radius. These results appear to indicate that end-pinching will not occur when $Oh = 0.01$ and that the breakdown of the calculations is purely numerical in origin. When the Ohnesorge number is lowered to $Oh = 5 \times 10^{-3}$ it is found that the radius of the neck closely follows the inviscid curve in figure 7. Until $t = 2.67$ (being the point at which the calculation breaks down due to mesh deformations) there is no sign that the rate at which the neck contracts slows down. This may indicate that end-pinching occurs.

	ν (m^2s^{-1})	ρ ($kg\,m^{-3}$)	γ ($N\,m^{-1}$)
Water	1.0×10^{-6}	1.0×10^3	7.2×10^{-2}
Benzene	0.6×10^{-6}	0.88×10^3	2.9×10^{-2}
Glycerol	1.0×10^{-3}	1.3×10^3	6.3×10^{-2}

TABLE 2. Physical constants for water, benzene and glycerol.

The foregoing suggests that the critical Ohnesorge number lies in the range $5 \times 10^{-3} < Oh^* < 10^{-2}$. It is difficult to be more precise about the value of Oh since a slow-down in the contraction rate of the neck is not a guarantee that the neck will not continue to contract. A clear sign of a steady neck radius (as in the case with $Oh = 0.01$) is not always obtained. It is interesting to look at experimental evidence which may support our belief that there is a critical Ohnesorge number below which end-pinching occurs. Hauser *et al.* (1936) investigated the evolution of pendant drops consisting of water, benzene and glycerol. In these experiments it was found that the radius of the filament formed when a drop breaks away from its point of attachment is almost independent of the value of the viscousity. Typically, the radius was found to be 0.25 mm. The recent experiments using water drops by Peregrine *et al.* (1990) yield a very similar value for the radius of the filament. The corresponding Ohnesorge numbers for water, benzene and glycerol (cf. table 2) are $Oh = 7.4 \times 10^{-3}$, $Oh = 6.6 \times 10^{-3}$ and $Oh = 8.9$ respectively. Note that the range in which we believe the critical Ohnesorge number to lie is of the same order as typical Ohnesorge numbers for low-viscosity filaments. In the experimental results of Hauser *et al.* (1936) the glycerol filament does not break up. This is as expected since the corresponding Ohnesorge number is three orders of magnitude larger than the region in which we believe the critical Ohnesorge number to lie. The water filament does not show breakup in either of the experiments by Hauser *et al.* (1936) or Peregrine *et al.* (1990). Interestingly, the benzene filament does break up into separate drops. Hence, if the breakup can be attributed to the mechanism described in the previous section the experimental evidence puts the critical Ohnesorge number in the range $6.6 \times 10^{-3} < Oh^* < 7.4 \times 10^{-3}$ which is within the bounds we obtained from our computations. Some caution is however required in accepting the narrow bounds for the critical Ohnesorge number as obtained from the experiments. There is simply insufficient experimental evidence to guarantee that the narrow bounds are not merely fortuitous.

Further care is required in attributing filament breakup as observed in the experiments by Hauser *et al.* (1936) to the Ohnesorge-number-dependent breakup mechanism which we have observed in our numerical work. While the estimate of the critical Ohnesorge number as obtained from the numerical computations agrees well with that obtained from the experiments, there may be other factors which may affect whether or not breakup occurs in experiments. The first effect which influences breakup is the initial aspect ratio of the filament. Our calculations have shown that for low-viscosity filaments, breakup will occur provided the filament is sufficiently long. If the filament is too short it will have contracted before axial undulations have grown so much that breakup occurs. From the numerical results we find that necking occurs after approximately 5 time units. One end of the filament contracts a distance of approximately 4 radii in this time span. Therefore, in order to prevent a full contraction before breakup a filament with an initial aspect ratio $\geqslant 8$ is required.

The photographs by Hauser *et al.* (1936) show only one instant in the evolution so that it is not possible to determine the initial length of the filaments from these photos. However, recent experiments by Zhang & Basaran (1995) show that a filament, formed when a drop of low-viscosity fluid breaks away from its point of attachment, has an aspect ratio $\geqslant 10$. This suggests that there is sufficient time for end-pinching to occur.

A second effect which may influence the breakup of the filament is the initial fluid motion inside the filament when it is formed. The situation we have assumed (no motion at $t = 0$) is highly idealized. For high-viscosity filaments the initial conditions are unlikely to be important since the time scale on which the filament contracts is large compared with the typical time scale on which short-wavelength initial disturbances will attenuate. For low-viscosity fluids this situation is different since disturbances associated with the formation of the filament may not have disappeared on the time scale on which end-pinching occurs. These disturbances may, in particular, lead to Rayleigh breakup before end-pinching occurs. The work of Lafrance (1975) shows that Rayleigh breakup is, in fact, unlikely to be able to compete with the end-pinching process. Namely, Lafrance showed that with an initial disturbance amplitude equal to 20% of the radius of an undisturbed (inviscid) jet, the dimensionless breakup time was of the order of 10 time units (decreasing the disturbance amplitude leads to a rapidly increasing breakup time). Recall that the breakup time due to the end-pinching process is approximately equal to 5 time units. This suggests that unless a large-amplitude disturbance is created with the correct wavelength, the Rayleigh breakup will be slower than the end-pinching process.

Transients associated with the formation of the filament may still influence end-pinching. In particular, transients with a wavelength approximately equal to that generated by the end-pinching process may be important. From figure 6 we note that the wavelength of the disturbance generated by the contracting end of the filament is approximately 3 radii long. From Bauer (1984) we obtain that the damping coefficient for a disturbance with a wavelength equal to 3 radii is approximated by $\delta = K \times Oh$ where $K \approx 50$. For shorter wavelengths K increases rapidly (halving the wavelength increases K by a factor of 3). For Ohnesorge numbers in the range of the critical value we find a damping coefficient of $\delta \approx 0.3$. Hence, in the 5 times units which are required for end-pinching to occur, the amplitude of disturbances with a wavelength equal to approximately 3 radii will have been reduced by at least 80%. These results indicate that even the transients with a wavelength most likely to affect the end-pinching process are unlikely to be of major importance.

5.2. *Rate of contraction*

From the results presented in the previous sections, it is clear that the Ohnesorge number has a major effect on the evolution of the filament. In order to investigate how the Ohnesorge number affects the rate of contraction of the filament we have plotted the curves of $\log(1 - L(t)/L_0)$ versus $\log(t)$ in figures 8(*a*) and 8(*b*) for the Ohnesorge numbers $Oh = 1, 0.1$ respectively. The different curves correspond to different values of L_0 as indicated in the plots. The dashed lines in figure 8 have a gradient equal to 2 while the gradient of the dot-dashed line in figure 8(*b*) is equal to 1. Let us consider figure 8(*a*). We observe that the curves have a slope which is approximately equal to 2 until the equilibrium configuration is reached. Hence, for $Oh = 1$ the end of the filament accelerates with an almost constant value, virtually until the equilibrium drop shape is attained.

When we consider figure 8(*b*) we observe that lowering the Ohnesorge number to

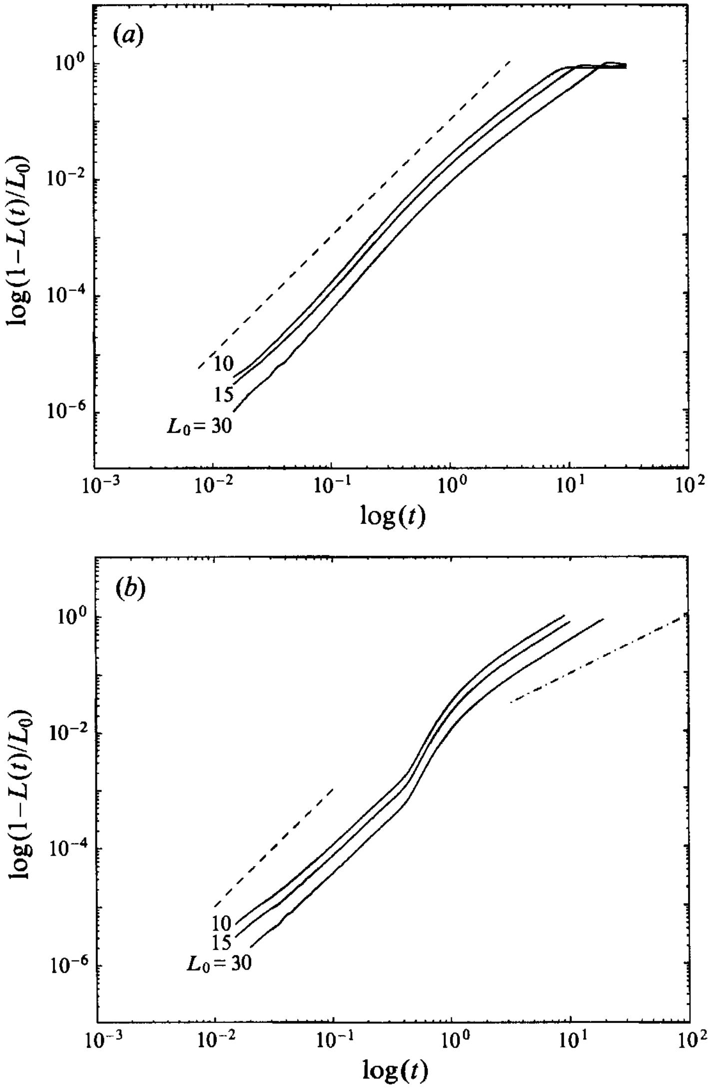

FIGURE 8. A plot of $\log(1 - L(t)/L_0)$ versus $\log(t)$ for the capillary numbers $Oh = 1$ (*a*) and $Oh = 0.1$ (*b*). The different curves in each plot correspond to the initial lengths $L_0 = 10, 15, 30$ as indicated. The dashed lines in both figures have a gradient equal to 2 while the dot-dashed line in (*b*) has a gradient equal to 1.

$Oh = 0.1$ leads to an interesting change in the contraction dynamics of the filament. For small times ($t < O(1)$) the slope of the lines is somewhat less than 2, indicating an almost constant acceleration of the end of the filament. We notice that for $t = O(1)$ the slope of the lines increases significantly, indicating an increase in the acceleration of the end of the filament. In fact, in this time interval we have $1 - L(t)/L_0 \sim t^{3.75}$. For still large times, $t = O(10)$, the slope of the lines decreases to a value of almost unity indicating that the end of the filament contracts with a constant velocity. As indicated in §4, we were not able to continue the calculation until the equilibrium configuration was reached in the case with $Oh = 0.1$. Therefore, figure 8(*b*) does not show the decelerating stage of the contraction.

In order to attempt to explain some of the above results it is instructive to investigate the evolution of the filament for $t \ll 1$. At the moment when the end of the filament just starts to move, a spherical cap with unit radius must be accelerated. In the initial instant, the only driving force present is the surface tension force. Since for small times the radius of the spherical cap may be assumed constant, it follows that neither the mass of the cap, nor the driving force will change. Hence, a constant force applied to a constant mass will lead to a constant acceleration of the mass. This corresponds with the behaviour seen in figure 8 for $t \ll 1$. While the foregoing argument may be able to explain the constant acceleration of the filament just after it started moving, we should stress that the argument is not valid for most of the time range shown in figure 8. That for $Oh = 1$ the filament has an almost constant acceleration for most of the time interval shown, is due to a non-trivial balance between surface tension forces on one hand and inertia and viscous forces on the other hand.

The increased rate of contraction when $t = O(1)$ and $Oh = 0.1$ has an interesting physical origin: in figure 7 we note that after $t = 0.5$ the neck ahead of the bulbous end of the filament starts to form. This implies that the time interval in which the increased acceleration occurs corresponds with the onset of the formation of the neck. Evidently, the bulbous end is drawn towards the neck when the neck forms, after which the rate of contraction slows down to an almost constant value. This observation lends support to the work of Keller (1983) and Ting & Keller (1990) who showed that the end of a uniform, inviscid filament contracting steadily advances with a constant velocity.

Results of calculations with smaller Ohnesorge numbers exhibit essentially the same behaviour as that observed for the case with $Oh = 0.1$: the early stage of steady acceleration is followed by an increased acceleration due to the formation of the neck. However, the stage in which the filament contracts with a steady velocity is not attained owing to end-pinching for sufficiently small Ohnesorge numbers.

6. Conclusions

In this paper we have studied the evolution of a free liquid filament which contracts under the action of surface tension forces. The Navier–Stokes equations in an axially symmetric geometry are solved numerically using a finite-element discretization procedure. Domain deformations are dealt with by means of a mixed Lagrangian–Eulerian approach. The capillary free surface is treated as Lagrangian so that nodes on the surface move with the convective velocity. Internal nodes are Eulerian–Lagrangian nodes. The position of these nodes is adjusted such that the movement of internal nodes reflects the topological change of the free surface.

The contraction characteristics are found to be crucially dependent on the Ohnesorge number Oh. For large Ohnesorge numbers ($Oh \geqslant O(1)$) the filament contracts uniformly without the occurrence of large velocity gradients inside the fluid domain. During the contraction a bulbous end is formed which grows slowly with time. The pressure in the fluid is mainly determined by the normal stress jump across the free surface which means that the point of minimum pressure coincides with the point of inflection of the free surface. End-pinching, the process of a drop breaking away from the end of the contracting filament, does not occur. The end of the contracting filament accelerates almost uniformly during most of the contracting stage. It is only when the ends of the filament approach the symmetry plane that the rate of contraction slows down.

When the Ohnesorge number is lowered we typically find that the bulbous end becomes more localized and ahead of the bulbous end a neck develops. In addition it is found that dynamic effects move the point of minimum pressure towards the neck. For Ohnesorge numbers in the range $10^{-2} \leqslant Oh \leqslant 10^{-1}$ a clear neck is visible but its radius reaches a steady value during the contraction. End-pinching therefore does not occur. For Ohnesorge numbers in this range the end of the filament accelerates uniformly during the unitial stage of the contraction. Subsequently, when the neck forms ahead of the bulbous end, the rate of contraction increases significantly. When the neck has formed the contraction reaches a stage in which the end of the filament moves with a constant velocity until the bulbous ends reach the symmetry plane.

Decreasing the Ohnesorge number to $Oh = 5 \times 10^{-3}$ we find that the contracting filament is no longer stable: end-pinching occurs. The mechanisms which lead to end-pinching are as follows. When the radius of the neck decreases the stress stress jump across the free surface increases in the necking region. In addition it is found that the pressure minimum in the fluid has moved towards the neck. The low-pressure region in the neck together with the large stress jump across the free surface combine to render the filament unstable, thus leading to end-pinching. The critical Ohnesorge number, Oh^*, that is, the Ohnesorge number below which end-pinching occurs, cannot be established with great precision due to the limitation of the numerical model. Numerically we find $5 \times 10^{-3} < Oh^* < 10^{-2}$. This value agrees well with experimental observations which put the critical Ohnesorge number in the range $6.6 \times 10^{-3} < Oh^* < 7.4 \times 10^{-3}$.

Two anonymous referees and Professor J. B. Keller have provided constructive comments which have improved clarity of the material presented in this paper. Extensive use was made of the finite-element package SEPRAN.

Appendix A. Eigenfrequencies of a viscous drop

The eigenfrequencies of a drop of liquid with an arbitrary viscosity were calculated by Reid (1960). It was shown that the eigenfrequencies are given by the roots of the following equation:

$$\frac{q_0^4}{q_l^4} + 1 = \frac{2(l-1)}{q_l^2}\left[l + (l+1)\frac{q_l - 2lQ_{l+1/2}}{q_l - 2Q_{l+1/2}}\right], \tag{A 1}$$

in which $q_l^2 = R^2\sigma_{l,\nu}/\nu$, $q_0^2 = R^2\sigma_{l,0}/\nu$ and $l = 1, 2, \cdots$. In these equations ν denotes the kinematic viscosity, R denotes the radius of the drop, $\sigma_{l,\nu}$ the eigenfrequency of the viscous drop, $\sigma_{l,0}$ the eigenfrequency of the inviscid drop and $Q_{l+1/2} = J_{l+3/2}(q)/J_{l+1/2}(q)$ in which $J_k(q)$ denotes Bessel functions of fractional order. We are interested in the roots of equation (A 1) for small values of the viscosity, that is, large q_l. Using asymptotic expressions for the Bessel functions (cf. Abramowitz & Stegun 1972) we find readily that $|Q_{l+1/2}| = O(1)$ so that after some manipulations we can approximate (A 1) by the equation

$$\sigma_{l,\nu}^2 + \sigma_{l,0}^2 - A\nu\sigma_{l,\nu} - B\nu^{3/2}\sigma_{l,\nu}^{1/2} + O(\nu^2) = 0, \tag{A 2}$$

in which $A = 2(l-1)(1+2l)/R^2$ and $B = 2(1-l^2)AQ_{l+1/2}/(1+2l)$. We next search for roots of (A 2) which have the form

$$\sigma_{l,\nu} = \mathrm{i}\sigma_l^{(0)} + \nu\sigma_l^{(1)} + \nu^{3/2}\sigma_l^{(2)} + O(\nu^2). \tag{A 3}$$

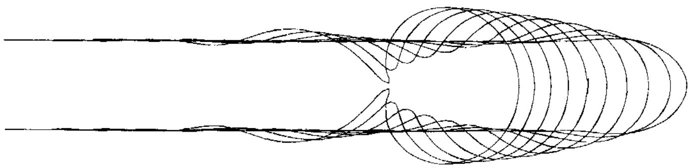

FIGURE 9. Free-surface shapes of a contracting inviscid filament with $L_0 = 15$. The free surfaces are shown at the times $t = 0.5(0.5)5.0$. The radius in the neck vanished at $t = 5.02$.

On substituting (A 3) into (A 2) and equating coefficients of like powers of ν equal to zero we find

$$\sigma_l^{(1)} = A/2, \qquad \sigma_l^{(2)} = \pm \frac{1-\mathrm{i}}{2^{3/2}\sigma_l^{(0)1/2}} B. \tag{A 4}$$

Since A is real, $\sigma_l^{(1)}$ is real. Thus, $\sigma_l^{(1)}$ denotes the leading-order approximation to the damping coefficient, which can also be obtained by alternative means (cf. Lamb 1945, §§275, 355). The correction to the leading-order approximations of the frequency and the damping coefficient is provided by $\sigma_l^{(2)}$. Using (A 2), (A 3) and the definition of q_l we find $q_l = \pm(\mathrm{i}+1)(\sigma_0^{(l)}/2\nu)^{1/2}R + O(\nu^{1/2})$. We are interested in the frequency and damping coefficient of the fundamental mode with $l = 2$. Using Abramowitz & Stegun (1972) we find that $Q_{5/2}(x) \rightarrow -\cot x$ in the limit $x \rightarrow \infty$. This result, together with the expression we have derived for q_2 yields

$$Q_{5/2} = \pm\mathrm{i} + O(\mathrm{e}^{-\nu^{1/2}}). \tag{A 5}$$

Thus, substituting the known expressions for $\sigma_l^{(1)}$ and $\sigma_l^{(2)}$ and employing the time and length scales as given in §2, we find the following approximation to the dimensionless frequency (ω) and the damping coefficient (δ) of a viscous drop oscillating in the fundamental mode,

$$\bar{\sigma}_{2,\nu} = \mathrm{i}\omega - \delta = \mathrm{i}\left[\sigma_2^{(0)} - \frac{3}{a^3}\left(\frac{2Oh^3}{\sigma_2^{(0)}}\right)^{1/2}\right] + \frac{5Oh}{a^2} - \frac{3}{a^3}\left(\frac{2Oh^3}{\sigma_2^{(0)}}\right)^{1/2} + O(Oh^2). \tag{A 6}$$

In (A6) a denotes the dimensionless radius of the drop in the undisturbed state and $\sigma_2^{(0)} = (8/a^3)^{1/2}$. When $a = (5/2)^{1/3}$ and $Oh = 0.05$, (A 6) yields $\omega = 1.775$ and $\delta = 0.122$.

Appendix B. Inviscid filament

In order to determine whether in the limit $Oh \rightarrow 0$ end-pinching occurs, we can use the fact that on the assumption of irrotational flow the equations for an inviscid fluid reduce to the Laplace equation for the velocity potential. This simplification has the benefit that an integral formulation exists for the Laplace equation. This implies that the problem for the velocity potential can be reduced to solving an integral equation prescribed only on the boundary of the domain of interest, which is of particular use in free-boundary problems. Employing the boundary-integral approach one is in particular more able to deal with large domain deformations on a local scale such as occur in a necking region. In this Appendix results obtained by means of a boundary-integral approach are presented for the case of a contracting inviscid filament. All details of this approach will be omitted since they can be found in Schulkes (1994*a*,*b*).

In figure 9 the domain of the inviscid liquid filament is plotted at the times indicated. Like in all calculations carried out in §4, it was assumed that at $t = 0$ the filament was at rest with the filament consisting of a cylindrical body with hemispherical ends. The initial length was taken to be $L_0 = 15$. We observe that the neck evolves slowly at first, but after $t = 4$ the radius of the neck decreases rapidly. End-pinching occurs after 5.02 time units.

REFERENCES

ABRAMOWITZ, M. & STEGUN, I. A. 1972 *Handbook of Mathematical Functions*. Dover.

BAUER, H. F. 1984 Natural damped frequencies of an infinitely long column of immiscible viscous fluids. *Z. Angew. Math. Mech.* **64**, 475–490.

CHEN, T.-Y. & TSAMOPOULOS, J. 1993 Nonlinear dynamics of liquid bridges: theory. *J. Fluid Mech.* **255**, 373–409.

CUVELIER, C., SEGAL, A. & VAN STEENHOVEN, A. A. 1986 *Finite Element Methods and Navier-Stokes Equations*. Reidel.

GOEDDE, E. F. & YUEN, M. C. 1970 Experiments on liquid jet instability. *J. Fluid Mech.* **40**, 495–511.

HAUSER, E. A., EDGERTON, H. E., HOLT, B. M. & COX, J. T. 1936 The application of the high-speed motion picture camera to research on the surface tension of liquids. *J. Phys. Chem.* **40**, 973–988.

HIRT, B. D. & NICHOLS, C. W. 1981 Volume of Fluid (VOF) method for the dynamics of free boundaries. *J. Comput. Phys.* **39**, 201–225.

HUERTA, A. & LIU, W. K. 1988 Viscous flow with large free surface motion. *Comput. Meth. Appl. Mech. Engng* **69**, 277–324.

JIANG, Y. J., UMEMURA, A. & LAW, C. K. 1992 An experimental investigation on the collision behaviour of hydrocarbon droplets. *J. Fluid Mech.* **234**, 171–190.

KELLER, J. B. 1983 Breaking of liquid films and liquid threads. *Phys. Fluids* **26**, 3451–3453.

KELLER, J. B., KING, A. & TING, L. 1995 Blob formation. *Phys. Fluids* **7**, 226–228.

LAFRANCE, P. 1975 Nonlinear breakup of a laminar liquid jet. *Phys. Fluids* **18**, 428–432.

LAMB, H. 1945 *Hydrodynamics*. Dover.

LAMBERT, J. D. 1991 *Numerical Methods for Ordinary Differential Systems*. Wiley.

MANSOUR, N. N. & LUNDGREN, T. S. 1990 Satellite formation in a capillary jet breakup. *Phys. Fluids* **2**, 1141–1144.

PEREGRINE, D. H., SHOKER, G. & SYMON, A. 1990 The bifurcation of liquid bridges. *J. Fluid Mech.* **212**, 25–39.

RAMASWAMY, B., KAWAHARA, M. & NAKAYAMA, T. 1986 Lagrangian finite-element method for the analysis of two dimensional sloshing problems. *Intl J. Numer Meth. Engng* **6**, 659–670.

REID, W. H. 1960 The oscillations of a viscous liquid drop. *Q. Appl. Maths* **18**, 86–89.

SCHULKES, R. M. S. M. 1994*a* The evolution of capillary fountains. *J. Fluid Mech.* **261**, 223–252.

SCHULKES, R. M. S. M. 1994*b* The evolution and bifurcation of a pendant drop. *J. Fluid Mech.* **278**, 83–100.

STONE, H. A. 1994 Dynamics of drop deformation and breakup in viscous fluids. *Ann. Rev. Fluid Mech.* **26**, 65–102.

STONE, H. A., BENTLEY, B. J. & LEAL, L. G. 1986 An experimental study of transient effects in the break up of viscous drops. *J. Fluid Mech.* **173**, 131–158.

STONE, H. A. & LEAL, L. G. 1989 Relaxation and break up of an initially extended drop in an otherwise quiescent fluid. *J. Fluid Mech.* **198**, 399–427.

TAYLOR, G. I. 1934 The formation of emulsions in definable fields of flow. *Proc. R. Soc. Lond.* A **146**, 501–523.

TING, L. & KELLER, J. B. 1990 Slender jets and thin sheets with surface tension. *SIAM J. Appl. Maths* **50**, 1533–1546.

TSAMOPOULOS, J. A. & BROWN, R. A. 1983 Nonlinear oscillations of inviscid drops and bubbles. *J. Fluid Mech.* **127**, 519–537.

ZHANG, X. & BASARAN, O. A. 1995 An experimental study of drop formation. *Phys. Fluids* **7**, 1184–1203.